

X-RAY OBSERVATION OF THE SHOCKED RED SUPERGIANT WIND OF CASSIOPEIA A

JAE-JOON LEE^{1,2} SANGWOOK PARK³, JOHN P. HUGHES⁴, AND PATRICK O. SLANE⁵*Draft version April 16, 2013*

ABSTRACT

Cas A is a Galactic supernova remnant, whose supernova explosion is observed to be of Type IIb from spectroscopy of its light echo (Krause et al. 2008). Having its SN type known, observational constraints on the mass loss history of Cas A's progenitor can provide crucial information on the final fate of massive stars. In this paper, we study X-ray characteristics of shocked ambient gas of Cas A using the 1 Msec observation with the *Chandra X-ray Observatory* (Hwang et al. 2004), and try to constrain the mass loss history of the progenitor star. We identify thermal emission from the shocked ambient gas along the outer boundary of the remnant. Comparison of measured radial variations of spectroscopic parameters of the shocked ambient gas to the self-similar solutions of Chevalier (1982) show that Cas A is expanding into a circumstellar wind rather than into a uniform medium. We estimate a wind density $n_H \sim 0.9 \pm 0.3 \text{ cm}^{-3}$ at the current outer radius of the remnant ($\sim 3 \text{ pc}$), which we interpret as a dense slow wind from a red supergiant (RSG) star. Our results suggest that the progenitor star of Cas A had an initial mass around $\sim 16 M_\odot$, and its mass before the explosion was about $5 M_\odot$, with uncertainties of a few tens of percent. Furthermore, the results suggest that, among the mass lost from the progenitor star ($\sim 11 M_\odot$), a significant amount (more than $6 M_\odot$) could have been via its RSG wind.

Subject headings: ISM: individual (Cas A) — supernova remnants — X-rays: ISM — stars: winds

1. INTRODUCTION

The mass of a star is the most crucial parameter that governs its structure, evolution and fate. Stellar masses vary throughout the life of stars: stars are subject to mass loss by winds and may experience mass exchange with their companion stars. For massive stars, in particular, mass loss plays a critical role in their evolution (e.g., Maeder et al. 2000), but this is poorly understood part of stellar evolution theory. Mass loss also profoundly impacts the eventual supernova (SN) explosion (Woosley et al. 2002) and the consequent evolution of the supernova remnant (SNR). Massive stars, with their strong ionizing radiation and powerful winds, clear out a large area around them throughout their lifetime (e.g., a radius larger than 15 pc for stars earlier than B0; Chevalier 1999). This implies that the immediate environment of a massive star is thus determined by the mass loss history of the star itself. It further implies that when the massive star undergoes core-collapse and explodes as a supernova, the supernova shocks expand inside the circumstellar structure. In other words, the structure and the evolution of “young” core-collapse SNRs reflects the pre-supernova mass-loss history of the progenitors, providing observational constraints on the nature of their progenitor stars.

Observations have established that stars with initial mass in the range $8 - 15 M_\odot$ undergo core collapse during their red supergiant (RSG) phases and produce Type II-

P SNe (Smartt et al. 2009). On the other hand, the fate of more massive stars is still not well established (e.g., see the discussion in Smith et al. 2011). For example, stars with masses of $15 - 30 M_\odot$ may explode during the RSG phase, producing Type II-L, IIb, or IIc SNe while stars with mass greater than $30 M_\odot$ may evolve into Wolf-Rayet stars and produce Type Ib or Ic SNe. But observational constraints on these associations are indirect and weak. Also, the fate of massive stars may be complicated by binary interactions.

For a star that undergoes a SN explosion during the RSG phase (or soon after it evolved past the RSG phase), its remnant will primarily interact with the surrounding RSG wind. Existence of such an RSG wind has been suggested for SN 1987A (Chevalier & Emmering 1989; Sugerman et al. 2005). The extent of the RSG wind would be determined by the location where the ram pressure of the wind equals the pressure of the surrounding medium. A radius of 5 pc is estimated for a canonical case (Chevalier 2005, $\dot{M} = 5 \times 10^{-5} M_\odot \text{ yr}^{-1}$, $v_w = 15 \text{ km s}^{-1}$, $p/k = 10^4 \text{ cm}^{-3} \text{ K}$). Thus, the interaction of the SNR with the RSG wind can last for thousands of years. The Galactic core-collapse SNR G292.0+1.8 is likely an example that is currently interacting with the RSG wind of its progenitor (Lee et al. 2010, LEE2010 hereafter). By analyzing the X-ray emission from the outer shock region of this ~ 3000 year-old SNR with the *Chandra X-ray* observatory, we found that the remnant has been expanding inside a wind. The estimated wind density ($n_H = 0.1 \sim 0.3 \text{ cm}^{-3}$) at the current outer radius ($\sim 7.7 \text{ pc}$) of the remnant is consistent with a slow wind from a RSG star.

Cas A, one of the best studied Galactic SNRs, also appears to be interacting with its RSG wind. At its age of about 330 yrs (Thorstensen et al. 2001, and references therein), its morphology and expansion rates

¹ Korea Astronomy and Space Science Institute, Daejeon 305-348, Korea

² leejjoon@kasi.re.kr

³ Department of Physics, University of Texas at Arlington Arlington, TX 76019

⁴ Department of Physics and Astronomy, Rutgers University, 136 Frelinghuysen Road, Piscataway, NJ 08854-8019

⁵ Harvard-Smithsonian Center for Astrophysics, 60 Garden Street, Cambridge, MA 02138

are consistent with a model SNR interacting with a RSG wind (Chevalier & Oishi 2003). It is also found that the observed characteristics of the X-ray ejecta knots are consistent with Cas A expanding into a wind (Laming & Hwang 2003; Hwang & Laming 2009). On the other hand, the direct identification of shocked RSG wind has been limited. The remnant contains slow moving shocked circumstellar clumps, called quasi-stationary flocculi (QSF). While earlier studies suggested that these could be fragments of the RSG shell swept-up by the later Wolf-Rayet wind, more recent studies favor that these are more likely dense clumps in the RSG wind (Chevalier & Oishi 2003). While observations have revealed detailed physical properties of these QSFs, the global characteristics of the RSG wind have not been well established so far.

The characteristics of the wind surrounding Cas A, i.e., the mass loss history of the progenitor of Cas A, is particularly pertinent as we know the supernova spectrum of Cas A at the time of its explosion from the light echo observations (Krause et al. 2008; Rest et al. 2011). The SN spectrum of Cas A shows that it is remarkably similar to that of SN 1993J, a prototypical Type IIb SN whose progenitor is likely a RSG star (Nomoto et al. 1993).

In this paper, we study the circumstellar environment of Cas A and try to constrain the mass loss history of the progenitor star. The basic method is similar to the one we applied to G292.0+1.8 in LEE2010, although here we use the 1 Msec Chandra observation of Cas A (Hwang et al. 2004). The data are briefly summarized in Section 2. In Section 3, we describe our detection of thermal X-ray emission from the shocked ambient gas and study its spectral characteristics. In Section 4, we show that the observed characteristics of the shocked ambient gas are consistent with those expected from a shocked RSG wind. Then the implication of our results on the nature of the progenitor star (Section 5) and cosmic ray acceleration (Section 6) is discussed. Section 7 summarizes our results.

2. DATA

Cas A was the first light target of the *Chandra* X-ray Observatory (Hughes et al. 2000), and has been observed multiple times with *Chandra*. The one million second exposure of Cas A was obtained with the ACIS-S3 detector on board *Chandra* in 2004 (Hwang et al. 2004). We use this one million second Chandra observation in our study. The 1 Msec observation data consist of 9 separate ObsIDs (4634, 4635, 4636, 4637, 4638, 4639, 5196, 5319 and 5320) with their exposure time ranging between ~ 40 ks and ~ 170 ks. We reprocessed the level 1 event files to create new level 2 event files. We applied parameters of the standard Chandra pipeline process, except that we turned off the pixel randomization. CIAO 4.2 and CALDB 4.2.2 were used for all the reprocessing and analysis.

3. ANALYSIS

3.1. Imaging Analysis

The X-ray emission from Cas A is dominated by emission from shocked metal rich ejecta. Along the outer boundary of Cas A are seen nonthermal filaments, which are synchrotron emission from the TeV electrons accelerated at the shock front (Reynolds 2008, for a recent

review). On the other hand, our study focuses on diffuse thermal emission from the shocked circumstellar gas that is expected to be fainter than the nonthermal emission. Although non-thermal X-ray filaments are seen along most of the outer boundaries, there are regions with weak non-thermal emission, especially in the northwest. The X-ray emission in these regions show no prominent limb-brightening, and we suspect that this is emission from shocked circumstellar wind.

The identification of the X-ray emission from shocked wind in Cas A is complicated not only due to non-thermal filaments but also due to contamination from ejecta emission. Furthermore, for the faint emission from shocked circumstellar gas, non-uniform backgrounds could be problematic. We consider two background components that are spatially varying, thus hindering the identification of the emission from the shocked circumstellar gas; they are out-of-time event⁶ along the CCD readout directions and a dust-scattered X-ray halo around bright sources (Overbeck 1965). In Cas A, both background components primarily originate from the bright ring of the shocked metal-rich ejecta, whose radius is about three quarters of the outer radius of the remnant. In the following, we describe our attempt to remove these two non-uniform background components. We note, however, that our intention of removing background components is to improve the “imaging” analysis of the faint emission from the outer shock region. For our spectral analysis, we use original data and the effect of these background components will be minimized by using the local background spectra.

To remove the contamination from out-of-time (OOT) events, we create OOT event files from level 1 event files following the method outlined in the M. Markevitch’s script `make_readout.bg`⁷. In short, this method substitutes chip-y (the readout direction) values of each event in the original level 1 event list with random ones, and processes them identically to the original event files (we refer them as OOT event files). From these OOT event files, we create OOT images. Then, the OOT images are subtracted from the image created using the original event files scaled for the ratio of the readout time over the frame time (0.041/3.2), resulting in the OOT-subtracted images.

The second background component considered is the dust-scattered X-ray halo emission, which is formed around an X-ray source due to small angle scattering by foreground dust particles (Mauche & Gorenstein 1989; Predehl & Schmitt 1995). Physical modeling of such emission, especially for an extended source, is complicated. It depends on the distribution of dust along the line-of-sight and the energy of the X-ray photons. Instead, we adopt a simple approach, where the spatial distribution of the halo emission is modeled as Gaussian profile around the source. In other words, the dust-scattered halo emission is estimated by ordinary Gaussian-convolution of the source image. The width and the amplitude of the convolution kernel are fitted to result in a flat background. This understated approach gives a poor approximation of the real halo emission near the source. However, we find that this provides a rea-

⁶ <http://cxc.harvard.edu/proposer/POG/html/chap6.html#sec:trailed-im>

⁷ <http://cxc.harvard.edu/contrib/maxim>

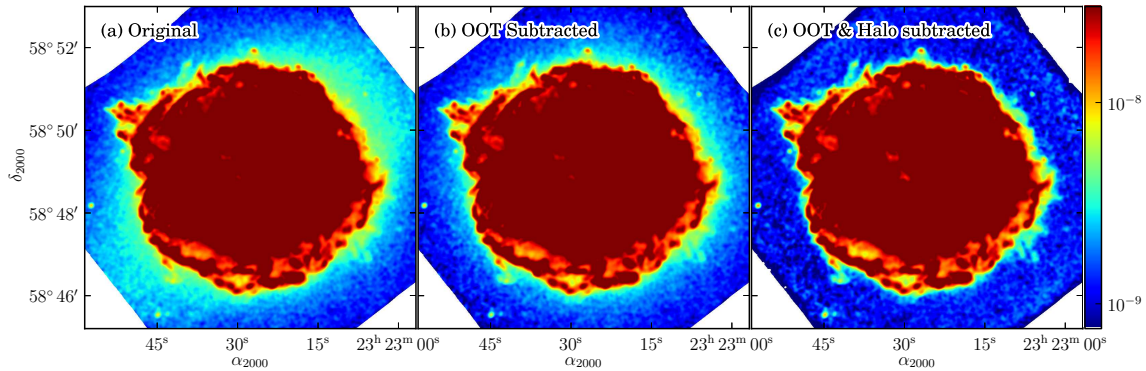


FIG. 1.— (a) Unprocessed Chandra image (3.34–7 keV) of Cas A. The image is smoothed with Gaussian beam of FWHM=4.5'' for better visualization. (b) Same Chandra image as in the left but with the out-of-time event subtracted (see the text for details). (c) Same Chandra image as in the center but the estimated dust scattered halo emission subtracted (see the text for details).

sonable approximation for the outer regions that we are interested in.

The steps of background subtraction are illustrated in Figure 1. The dominant background contribution in the original image (Figure 1(a)) is the OOT contribution seen along the direction of northwest to southeast which is the readout direction. The OOT contribution is effectively removed in the OOT-subtracted image (Figure 1(b)) while the remaining halo emission is clearly visible. And we see that the halo contribution is significantly reduced in our final image (Figure 1(c)). We note that the results depend on the chosen energy band. We find that the energy range of 3.34 – 7 keV, which does not include any prominent metal lines, provides the best result. In softer energy ranges, the strong line emission from the shocked metal-rich ejecta makes the background subtraction less optimal.

In Figure 2, we reproduce the Figure 1(c) in false-color with different contrast. It clearly shows the existence of faint diffuse emission around the outer boundary of Cas A. The nonthermal emission is relatively weak in the western boundary where the emission shows a faint plateau. In contrast to the non-thermal filaments, little hint of limb-brightening is seen in this region. The emission without the limb-brightening is indeed what one would expect from the thermal emission of the shocked

ambient gas when the remnant is expanding into a wind, as demonstrated in the case of G292.0+1.8 (LEE2010), and they are promising candidate emission features from shocked circumstellar wind. We note that this emission, in projection, often extends beyond the nonthermal filaments which marks the location of the outer shock front. To test if the faint emission beyond the nonthermal filaments is real and not some artifacts of our background subtraction, we extract radial intensity profiles in several regions from the original image and also from the background-subtracted image. White lines in Figure 2 are the regions where the radial profiles are extracted (these regions are associated with the regions where spectra are extracted in Section 3.2), and their radial profiles are shown in Figure 3. For each profile in Figure 3, we mark the locations of the outer shock front that we visually identified from the background-subtracted image (Figure 2). We find that the profiles extracted from the original image do show changes in their slope across the proposed boundaries, indicating they are real. As will be discussed in the next section, spectra of these regions confirm their ambient origin.

3.2. Spectral Analysis

We extract spectra from several regions around the outermost boundary believed to be dominated by thermal emission of shocked ambient gas. The extraction regions are shown in Figure 4 and the corresponding spectra are shown in Figure 5. The spectra are extracted from the original event files, thus the processes described in Section 3.1 do not apply for the spectral analysis. Instead, the background spectra are extracted from the regions right outside the boundary, therefore the contribution of the OOT event and the halo emission to the source spectra is should be negligible. We selected regions with little contamination from the ejecta emission and the nonthermal emission. The spectra of these regions clearly show Silicon and Sulfur lines. The overall spectral slope in the hard part of spectra is also softer than that of the nonthermal filament (an example spectrum of nonthermal filament is also shown in Figure 5 for a comparison). Therefore, we conclude that the X-ray emission we have extracted is dominated by a thermal component.

The extracted spectra are fit with a single nonequilibrium ionization plane-parallel shock model (vpshock in Xspec v12, Borkowski et al. 2001) with varying abun-

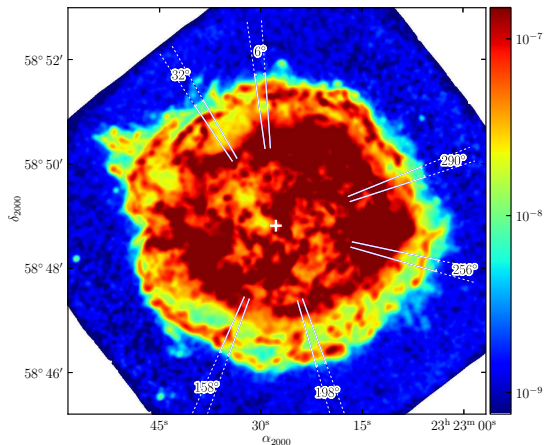


FIG. 2.— Background subtracted Chandra image (3.34–7 keV) of Cas A smoothed with Gaussian beam of FWHM=4.5''. White lines are the areas where the radial profiles in Figure 3 are extracted and labels mark their position angles.

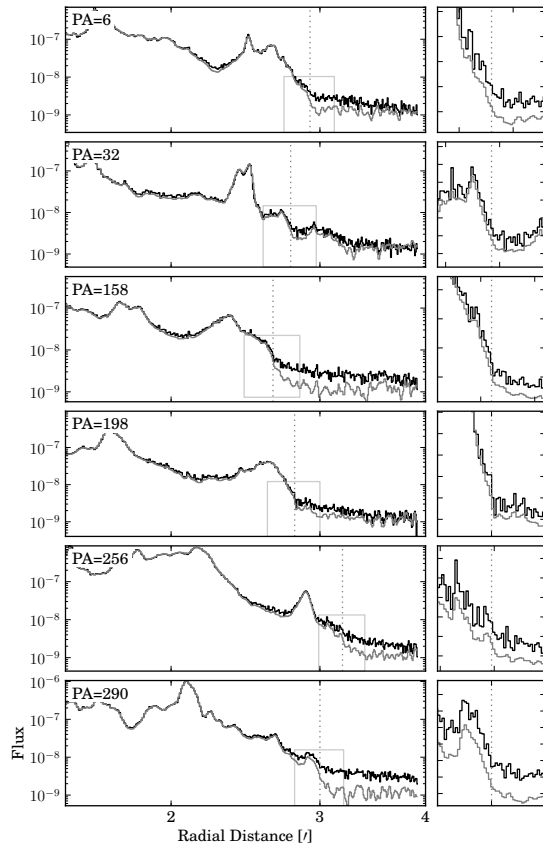


FIG. 3.— Radial intensity profiles ($E=3.34 \sim 7$ keV) extracted along the several regions shown in Figure 2. The black lines are from original image and the gray lines are from background subtracted image. The left panels show the radial profile in a log-log scale. The right panels show the same radial profiles in a linear-linear scale for the region near the outer boundary (marked as gray boxes on the left panes). The locations of the outer boundary visually identified from Figure 2 are marked as vertical dashed lines.

dances. The spectra are not binned, instead we use Churazov weighting (Churazov et al. 1996). The net photon count for each spectrum is between 5,000 and 20,000 photons. The best fit models are overlaid in Figure 5. We find that a single vps shock model adequately fits the observed spectra. The fitted abundances are similar to or less than the solar values. A similar low abundance pattern has been also found from the outer shock of G292.0+1.8 (LEE2010). Therefore we suggest that the faint emission we see is thermal emission from shocked ambient gas. In Table 1, we summarize the fit parameters for each region, sorted by their position angle (P.A.). Throughout this paper, we adopt the explosion center from Thorstensen et al. (2001) as the remnant center. It is possible that there is some contribution from the nonthermal emission, and any residual nonthermal component would affect the fit parameters. We note that fitting the spectra with additional powerlaw component (with its photon index fixed at 2.5 from the fit to nearby nonthermal filaments) decreases the fitted temperature while increasing the ionization time scale, but other parameters remain consistent within their error ranges.

In Figure 6, we compare spectral parameters of each region as a function of their position angles. The absorbing hydrogen column densities and electron temperatures are given from the spectral fit. The densities are estimated

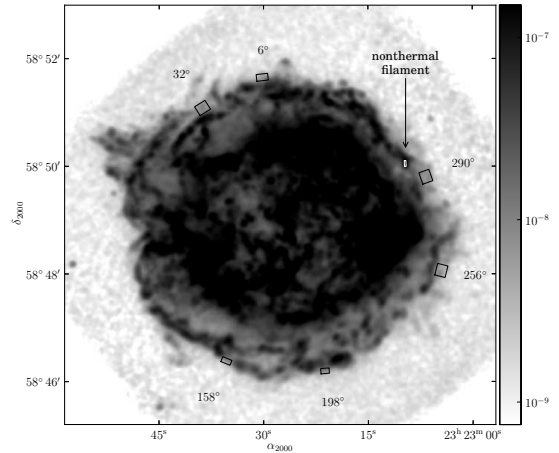


FIG. 4.— Regions where the azimuthal spectra in Figure 5 are extracted. The regions are labeled by their position angles from the remnant center.

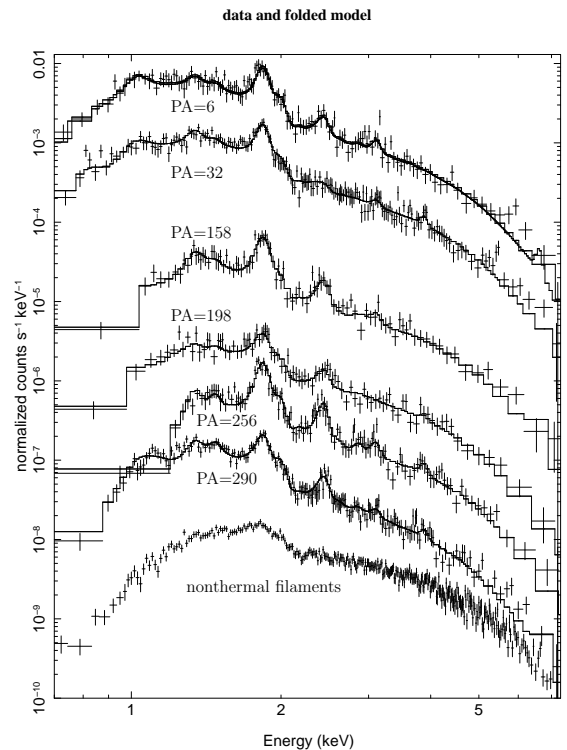


FIG. 5.— Extracted Chandra spectra of the outer faint regions in Figure 4 and their best fit models. The bottom spectrum is from the nonthermal filament also marked in Figure 4, shown for comparison.

from the fitted volume emission measures. The volume corresponding to each region is calculated by pixel-by-pixel integration of the path-lengths over the projected area. In this calculation, we assumed a sphere centered at the assumed center of the remnant at a distance of 3.4 kpc (Reed et al. 1995). The radius of the sphere is separately determined for each region as the projected distance of the farthest (from the assumed center of the remnant) pixel in the region. The absorbing hydrogen column densities seem relatively low in the north compared with other directions, which seems consistent with the results of Hwang & Laming (2012). On the other

TABLE 1
X-RAY SPECTRAL PARAMETERS OF THE REGIONS USED IN THE AZIMUTHAL ANALYSIS.

P.A. [†] [°]	Area '' ²	N_H [10^{22} cm ⁻²]	kT_e [keV]	norm [10^{-19} cm ⁻⁵]	$n_e t$ [10^{11} cm ⁻³ s]	Ne	Mg	Si	S	Ca	Fe	reduced χ^2_{\dagger}
6	399	$0.9^{+0.1}_{-0.1}$	$2.3^{+0.3}_{-0.3}$	$9.7^{+2.1}_{-1.5}$	$1.9^{+0.7}_{-0.5}$	$0.2^{+0.3}_{-0.2}$	$0.2^{+0.1}_{-0.1}$	$0.4^{+0.1}_{-0.1}$	$0.3^{+0.1}_{-0.1}$	$0.0^{+0.6}_{-0.0}$	$0.2^{+0.2}_{-0.1}$	0.90
32	655	$1.0^{+0.1}_{-0.1}$	$2.1^{+0.1}_{-0.2}$	$22.7^{+1.5}_{-1.8}$	$1.5^{+0.3}_{-0.3}$	$0.0^{+0.1}_{-0.0}$	$0.1^{+0.1}_{-0.0}$	$0.3^{+0.1}_{-0.1}$	$0.1^{+0.1}_{-0.1}$	$0.8^{+0.7}_{-0.7}$	$0.1^{+0.0}_{-0.1}$	1.03
158	269	$1.9^{+0.3}_{-0.3}$	$2.2^{+0.4}_{-0.4}$	$8.6^{+2.0}_{-1.9}$	$1.5^{+0.5}_{-0.3}$	$0.0^{+0.0}_{-0.0}$	$0.5^{+0.5}_{-0.2}$	$0.7^{+0.2}_{-0.2}$	$0.5^{+0.2}_{-0.2}$	$0.0^{+1.2}_{-0.0}$	$0.9^{+0.5}_{-0.5}$	1.01
198	228	$1.2^{+0.5}_{-0.2}$	$2.3^{+0.4}_{-0.4}$	$8.1^{+3.2}_{-1.6}$	$1.9^{+1.9}_{-0.8}$	$0.2^{+0.5}_{-0.2}$	$0.1^{+0.1}_{-0.1}$	$0.2^{+0.1}_{-0.1}$	$0.2^{+0.8}_{-0.2}$	$0.3^{+0.8}_{-0.3}$	$0.0^{+0.4}_{-0.0}$	0.94
256	645	$1.6^{+0.3}_{-0.2}$	$2.2^{+0.4}_{-0.3}$	$17.3^{+5.6}_{-3.0}$	$2.0^{+0.6}_{-0.4}$	$0.0^{+0.8}_{-0.0}$	$0.5^{+0.2}_{-0.2}$	$0.9^{+0.3}_{-0.2}$	$0.7^{+0.1}_{-0.2}$	$0.9^{+0.8}_{-0.9}$	$0.0^{+0.2}_{-0.0}$	1.11
290	655	$1.3^{+0.2}_{-0.1}$	$1.8^{+0.1}_{-0.2}$	$34.7^{+5.8}_{-3.9}$	$4.0^{+0.9}_{-0.9}$	$0.0^{+0.5}_{-0.0}$	$0.4^{+0.2}_{-0.1}$	$0.5^{+0.1}_{-0.1}$	$0.3^{+0.1}_{-0.1}$	$0.6^{+0.5}_{-0.5}$	$0.4^{+0.2}_{-0.1}$	1.02

[†] Position angles to each region are measured east of north from the geometrical center.

[‡] For all individual spectra, the degree of freedom (ν) is 454.

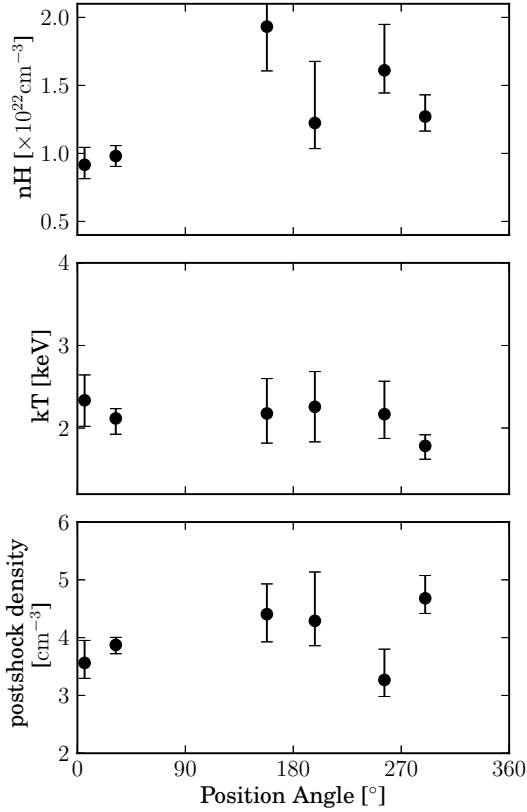


FIG. 6.— Azimuthal distribution of the absorbing column densities (top), electron temperatures (middle) and the postshock densities (bottom) from the spectral fits of the outermost regions in Figure 5.

hand, we could not see a clear azimuthal trend in the electron temperatures and the hydrogen densities. Similarly, Figure 7 shows variation of the electron temperatures and the hydrogen densities of each region as a function of their distance from the remnant center. No clear indication of radial trends is noticed although the radius range that we are sampling is rather limited ($2.7' \lesssim R \lesssim 3.2'$).

As has been demonstrated in the case of G292.0+1.8 (LEE2010), one can investigate the radial structure of the “shocked” ambient gas to test whether the gas is of interstellar origin or of circumstellar origin. We note that the radial structure we are considering here is qualitatively different from what is shown in Figure 7, which

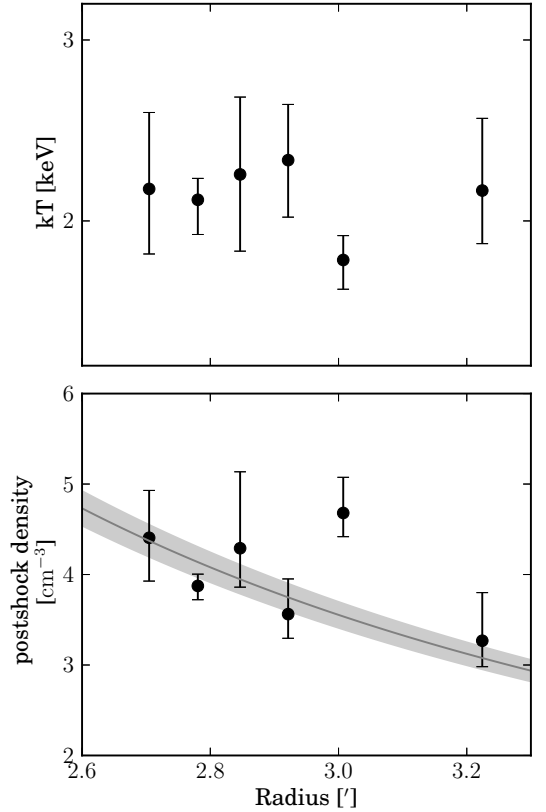


FIG. 7.— Electron temperatures (top) and the postshock densities (bottom) from the spectral fits of the outermost regions in Figure 5 are plotted as a function of their radial distances from the center. If Cas A is expanding inside a wind, the radial variation of postshock density in this figure will follow the preshock density profile scaled by the shock compression ratio. The solid line is the best fit model with a simple wind profile ($\rho \propto r^{-2}$) and the gray area represents the formal error of the fit for 90% confidence interval.

represents characteristics of “multiple” shocks of different directions (and at different radii from the center). By radial structure, we mean radial variations of gas characteristics behind “a” shock, which represents accumulated history of shock propagation. Investigating the nature of ambient gas from the radial structure behind a shock requires a radial series of spectra that covers large enough radial range to test different models. We select regions in the northwestern boundary where emission from the nonthermal filaments is insignificant. Figure 8 shows the

regions where we extract the radial series of spectra. We allow the area of the regions to increase outwardly to compensate for decreasing surface brightness. Again, the background spectra are extracted from the regions right outside the shock boundary. In the inner region away from the shock boundary, the contribution of the OOT event and the halo emission may remain in the source spectra. However, we do not think that significantly affects our analysis because, as will be shown later, the emission from the CSM itself is much strong in this inner region. The spectra of individual regions are first fit independently as in the azimuthal analysis. The fitted metal abundances are found to be less than those of solar values, even in the bright innermost region well inside the remnant boundary. This suggests that most emission (if not all) of our selected regions is from shocked ambient gas. The fitted absorbing column densities (N_{H}) of these regions were consistent within their uncertainties. We consider that the variation of N_{H} in this small patch of the sky is negligible compared to uncertainties in the fit parameters and we refit the whole set of spectra with N_{H} fixed at the value of $1.2 \times 10^{22} \text{ cm}^{-2}$, an average from the independent fits. Figure 9 shows a selected sample of the spectra from these regions and their best fit models. And the fit results are summarized in Table 2 and plotted in Figure 10. It is clear that the observed emission measure monotonically increases toward the remnant center. On the other hand, the variation of the electron temperature is complicated. In the inner regions (radius smaller than $2.5'$), we see clear tendency of inwardly decreasing electron temperature. But the temperature remains more or less flat in the outer regions (radius between $2.5' \sim 3.0'$). For some elements (e.g., Ne, Mg, and Si), their abundances are higher for the inner regions. However, it is not clear whether this trend is real or is due to some systematic uncertainties. The radial structure behind the shock will be further discussed in the next section.

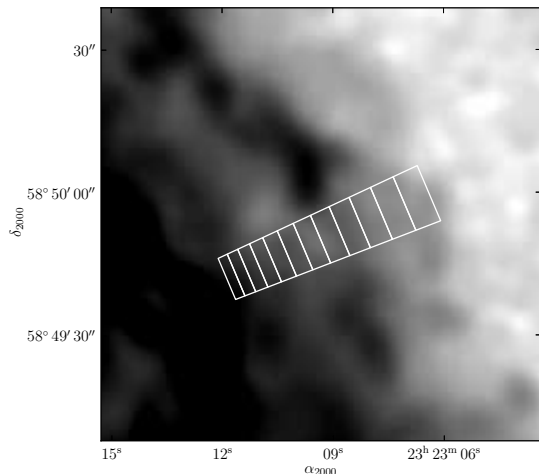


FIG. 8.— Zoomed view of the northwestern part of Figure 2 with regions for the radial spectral analysis are marked as white boxes.

4. NATURE OF THE AMBIENT GAS

The radial structure of the shocked ambient gas can trace the radial density structure of the medium into which the remnant is expanding. Chevalier (1982) found

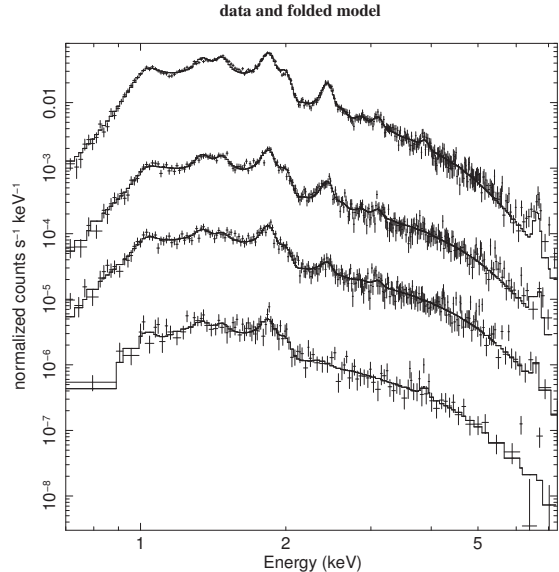


FIG. 9.— Sample of Chandra spectra extracted from regions for the radial analysis in Figure 8. The uppermost spectra corresponds to the innermost region, and the lowermost spectra to the outermost region. Their best fit models are also shown.

self-similar solutions for the interaction of expanding stellar ejecta ($\rho \propto r^{-n}$, $n > 5$) with an external medium ($\rho \propto r^{-s}$) where s and n are the power law index of the density profile for ambient gas and for the ejecta, respectively: a remnant expanding in a uniform ambient medium ($s = 0$) would result in an inward-decreasing density and an inward-increasing temperature profile of shocked ambient gas, while a remnant expanding in a medium with a wind profile ($s = 2$) would show an inward-increasing density and an inward-decreasing temperature. The primary effect of n (the density structure of the ejecta) to the solution is change in the distance between the forward shock and the contact discontinuity, and does not fundamentally change the overall behavior. Therefore, by studying the current radial profile of the density and temperature of shocked ambient gas, one can infer whether the SNR has been expanding in a density gradient. The utility of this method has been successfully demonstrated in our study of Galactic core-collapse SNR G292.0+1.8 (LEE2010).

In Figure 10, we overlay model predicted radial structure of the temperature and emission measure on top of the observed ones. We adopt self-similar solutions of Chevalier (1982) and project them assuming a spherical geometry. As in LEE2010, the projected temperature is taken as an average temperature along the line of sight weighted by density squared, ignoring the variation in the intrinsic emissivity of the gas at different temperatures.

The increasing emission measure toward the remnant center, as can be seen from Figure 10, is the behavior expected for the remnant expanding inside a wind and we find that the observation is consistent with self-similar solutions with $s = 2$ and $6 < n < 7$. The temperature variation is not consistent with any of the models, although the decrease in temperature in the inner part ($R \lesssim 2.5 \text{ pc}$) is what is expected in the $s = 2$ models. As will be discussed below, direct comparison between observed temperature to model ones is difficult due to complicated shock physics, especially near the shock front. On the

TABLE 2
X-RAY SPECTRAL PARAMETERS OF THE REGIONS USED IN THE RADIAL ANALYSIS.

Distance [']	Area '' ²	kT_e [keV]	norm [10^{-19} cm^{-5}]	$n_e t$ [$10^{11} \text{ cm}^{-3} \text{ s}$]	Ne	Mg	Si	S	Ca	Fe	reduced χ^2 [†]
2.22	69	$1.5^{+0.1}_{-0.1}$	$85.4^{+6.6}_{-3.8}$	$9.2^{+1.6}_{-1.2}$	$0.7^{+0.2}_{-0.2}$	$0.8^{+0.1}_{-0.1}$	$0.8^{+0.1}_{-0.1}$	$0.7^{+0.1}_{-0.1}$	$0.6^{+0.3}_{-0.3}$	$0.4^{+0.1}_{-0.1}$	1.24
2.26	82	$1.4^{+0.1}_{-0.1}$	$92.5^{+5.0}_{-5.8}$	$10.6^{+1.3}_{-1.4}$	$1.0^{+0.3}_{-0.2}$	$0.8^{+0.1}_{-0.1}$	$0.7^{+0.1}_{-0.1}$	$0.7^{+0.1}_{-0.1}$	$0.6^{+0.8}_{-0.6}$	$0.3^{+0.1}_{-0.1}$	1.29
2.30	97	$1.5^{+0.1}_{-0.1}$	$65.8^{+5.6}_{-4.2}$	$6.0^{+1.0}_{-0.7}$	$1.0^{+0.3}_{-0.2}$	$0.7^{+0.1}_{-0.1}$	$0.6^{+0.1}_{-0.1}$	$0.6^{+0.1}_{-0.1}$	$0.4^{+0.3}_{-0.3}$	$0.3^{+0.1}_{-0.1}$	1.36
2.34	111	$1.6^{+0.1}_{-0.1}$	$45.6^{+4.5}_{-3.0}$	$5.6^{+1.0}_{-0.8}$	$1.1^{+0.2}_{-0.3}$	$0.8^{+0.1}_{-0.1}$	$0.8^{+0.1}_{-0.1}$	$0.6^{+0.1}_{-0.1}$	$0.8^{+0.8}_{-0.8}$	$0.4^{+0.1}_{-0.1}$	0.99
2.39	125	$1.8^{+0.1}_{-0.1}$	$31.9^{+2.7}_{-2.4}$	$4.1^{+0.8}_{-0.6}$	$0.7^{+0.3}_{-0.3}$	$0.5^{+0.1}_{-0.1}$	$0.6^{+0.1}_{-0.1}$	$0.5^{+0.1}_{-0.1}$	$0.3^{+0.8}_{-0.3}$	$0.4^{+0.1}_{-0.1}$	1.01
2.44	142	$2.1^{+0.1}_{-0.1}$	$25.5^{+2.4}_{-2.0}$	$3.7^{+0.7}_{-0.6}$	$0.4^{+0.3}_{-0.3}$	$0.6^{+0.1}_{-0.1}$	$0.6^{+0.1}_{-0.1}$	$0.5^{+0.1}_{-0.1}$	$0.0^{+0.4}_{-0.1}$	$0.4^{+0.1}_{-0.1}$	1.01
2.50	160	$2.3^{+0.2}_{-0.1}$	$21.9^{+1.7}_{-1.8}$	$3.8^{+0.8}_{-0.6}$	$0.5^{+0.4}_{-0.3}$	$0.6^{+0.1}_{-0.1}$	$0.5^{+0.1}_{-0.1}$	$0.3^{+0.1}_{-0.1}$	$0.2^{+0.5}_{-0.2}$	$0.4^{+0.1}_{-0.1}$	1.19
2.56	177	$2.1^{+0.1}_{-0.1}$	$16.3^{+2.4}_{-2.0}$	$3.1^{+0.9}_{-0.6}$	$0.7^{+0.5}_{-0.4}$	$0.4^{+0.2}_{-0.1}$	$0.5^{+0.1}_{-0.1}$	$0.2^{+0.1}_{-0.1}$	$0.0^{+0.5}_{-0.1}$	$0.4^{+0.1}_{-0.1}$	0.94
2.63	197	$2.0^{+0.1}_{-0.1}$	$24.7^{+2.2}_{-2.4}$	$2.6^{+0.5}_{-0.4}$	$0.0^{+0.3}_{-0.1}$	$0.2^{+0.1}_{-0.1}$	$0.3^{+0.1}_{-0.1}$	$0.2^{+0.1}_{-0.1}$	$0.2^{+0.5}_{-0.2}$	$0.4^{+0.1}_{-0.1}$	1.01
2.71	217	$2.3^{+0.2}_{-0.2}$	$22.0^{+1.9}_{-1.8}$	$2.2^{+0.5}_{-0.4}$	$0.2^{+0.3}_{-0.2}$	$0.2^{+0.1}_{-0.1}$	$0.3^{+0.1}_{-0.1}$	$0.2^{+0.1}_{-0.1}$	$0.0^{+0.3}_{-0.1}$	$0.3^{+0.1}_{-0.1}$	1.01
2.79	240	$1.8^{+0.1}_{-0.1}$	$17.7^{+2.9}_{-2.3}$	$3.6^{+1.8}_{-1.1}$	$0.9^{+0.8}_{-0.6}$	$0.3^{+0.2}_{-0.1}$	$0.3^{+0.1}_{-0.1}$	$0.1^{+0.1}_{-0.1}$	$0.2^{+0.7}_{-0.2}$	$0.2^{+0.1}_{-0.1}$	0.96
2.87	260	$1.8^{+0.3}_{-0.2}$	$14.6^{+3.0}_{-3.1}$	$2.8^{+1.6}_{-0.8}$	$0.8^{+0.8}_{-0.5}$	$0.3^{+0.2}_{-0.1}$	$0.3^{+0.1}_{-0.1}$	$0.3^{+0.2}_{-0.1}$	$0.9^{+0.8}_{-0.8}$	$0.1^{+0.2}_{-0.1}$	0.91
2.96	288	$1.9^{+0.3}_{-0.2}$	$10.6^{+2.2}_{-2.2}$	$3.8^{+4.4}_{-1.7}$	$0.7^{+1.2}_{-0.7}$	$0.3^{+0.8}_{-0.3}$	$0.3^{+0.8}_{-0.3}$	$0.0^{+0.2}_{-0.1}$	$0.8^{+1.0}_{-0.8}$	$0.1^{+0.2}_{-0.1}$	0.96

[†] For all individual spectra, the degree of freedom (ν) is 455.

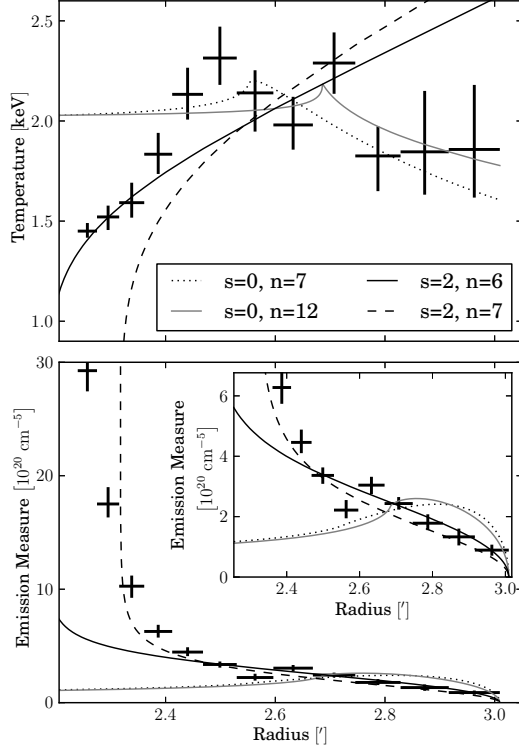


FIG. 10.— Fitted electron temperatures and emission measures of the radial series spectra of Figure 9, plotted as a function of their radial distances from the center. Lines are model predictions from Chevalier (1982; see Section 4 for more details) for different sets of parameters, where s and n are power-law index for the density profile of the ambient medium and of the expanding ejecta, respectively. The temperatures and emission measures of the model predictions have been scaled to match the observed values. The inset of the bottom panel shows same data with different scales. For the models of $s = 0$, contact discontinuity is marked by cusps in the temperature profile. For the models of $s = 2$, contact discontinuity is where the temperature drops to zero and the emission measure diverges to infinity.

other hand, the fact that the observed variation of the emission measure is in good agreement with models of $s = 2$ clearly suggest that the density of the ambient

gas radially decreases, which confirms that Cas A has been expanding inside the wind. While our data suggest a power-law index n of ejecta envelop between 6 and 7, this may not be a reliable estimate as has been discussed in LEE2010. We note, however, that Laming & Hwang (2003) studied ejecta emission in Cas A and found n between 6 to 7.

The temperatures from our X-ray spectral fits are electron temperatures, while the temperatures of the models are ion temperatures. These two can differ considerably in non-radiative shocks faster than 1000 km s^{-1} (e.g., Ghavamian et al. 2007, and references therein). The shock velocity measured from the proper motion of non-thermal filaments is about 5000 km s^{-1} (DeLaney et al. 2004), while the measured electron temperature ranges between 2 to 2.5 keV (Table 1). This corresponds to $T_e/T_p = 0.05$, assuming all the shock energy has converted into the energy of the ordinary gas (i.e., no cosmic ray acceleration; however, see Section 6). Previous studies suggested that, for fast shocks ($v_s \gtrsim 1000 \text{ km s}^{-1}$), the temperature equilibration between electrons and protons are low ($T_e/T_p \lesssim 0.1$) and possibly scales with v^{-2} (Ghavamian et al. 2007). The observed electron temperature in Cas A and its inferred T_e/T_p , assuming no cosmic ray acceleration, seems to be consistent with observed values of other SNRs. Since it has been known that there is CR acceleration in Cas A, it is likely that the observed low electron temperature is partially due to an efficient cosmic ray acceleration at the forward shock (e.g., Vink & Laming 2003). Nevertheless, the measured electron temperature is likely not to trace the temperature expected from the self-similar solutions of Chevalier (1982) and the discrepancy between the models and the observed values likely represent incomplete physics of the self-similar models we used. However, while efficient cosmic ray acceleration may affect some of our results, e.g., estimated preshock densities, we do not consider the effects to be highly significant in the sense that they will not invalidate our primary result that Cas A has been expanding inside its wind.

The properties of shocked ambient gas we estimated in

Section 3.2 are therefore the properties of wind material. The measured postshock densities in Figure 7 are from regions around the outermost boundary for different position angles, and the self-similar solutions of Chevalier (1982) show that the density remains flat near the shock front. Thus, we consider these measured densities closely approximate wind densities at the location of the forward shock, scaled by the assumed postshock compression ratio. Fitting the observed densities in Fig. 7(b) with a wind profile assuming a constant postshock compression ratio of 4 gives a wind density profile of

$$n_{\text{H}} = 0.89 \left(\frac{r}{3 \text{ pc}} \right)^{-2} \text{ cm}^{-3}.$$

The formal error from the fit (for 90% confidence interval) is about 5%. However, given the scatter of density values for individual regions, which may reflect the asymmetric nature of the wind, an error of 30% would be more realistic. The inferred density profile of Cas A corresponds to the mass loss rate of

$$\dot{M} = 2.5 \times 10^{-5} \left(\frac{v_w}{10 \text{ km s}^{-1}} \right) \text{ M}_{\odot} \text{ yr}^{-1}.$$

where v_w is the wind velocity. The mass loss rate is too large to be that of the WR wind ($\dot{M} > 10^{-3} \text{ M}_{\odot} \text{ yr}^{-1}$ for $v_w > 1000 \text{ km s}^{-1}$) and consistent with that of the RSG wind estimated from SNe studies (e.g., Sramek & Weiler 2003). Therefore, our results support that Cas A is currently expanding within the RSG wind. Using the morphology and expansion rates of Cas A, Chevalier & Oishi (2003) estimated explosion energy (E) and the total mass of the ejecta (M_e), but as a function of the wind density. Substituting our observed wind density, we get $E = 5 \times 10^{51} \text{ erg}$ and $M_e = 4 \text{ M}_{\odot}$. And the observed mass of the swept-up wind is around 6 M_{\odot} . For all these estimates, the uncertainties of our density estimate will propagate linearly, thus we expect about 30% of uncertainties. Note that these estimates may be further subject to systematic uncertainties. For example, these values are calculated assuming the RSG wind had a constant mass loss rate, and will be affected by a possible time variation of the mass loss rate. It was proposed that the dense wind of Cas A may not have extended directly to the surface of the progenitor star and Cas A might have exploded into a low density bubble (e.g., Krause et al. 2008). However, Schure et al. (2008) and Hwang & Laming (2009) found that the size of the bubble, if it existed, would not have been larger than 0.3 pc, which is significantly smaller than the current radius of Cas A ($\sim 3 \text{ pc}$). Therefore, the effect of the bubble on our estimates does not seem significant. Vink et al. (1996) and Favata et al. (1997) derived a total swept up mass ranging from 5 to 9 M_{\odot} using the global X-ray spectrum of Cas A. While this is in agreement with ours, the mass estimates based on the fits to the global X-ray spectrum may suffer from uncertainties due to the spatial variation of X-ray spectra and the contribution from shocked ejecta.

5. PROGENITOR OF Cas A

A lower limit on the progenitor's initial mass can be estimated by combining all the masses associated with Cas A. If we combine the shocked wind mass ($\gtrsim 6 \text{ M}_{\odot}$),

the ejecta mass (4 M_{\odot}), and the mass of the neutron star ($\sim 1.4 \text{ M}_{\odot}$), we estimate the initial mass of the progenitor at least larger than 11 M_{\odot} . Another estimate of the initial mass comes from the SN type of Cas A. The SN spectra of Cas A observed by the light echos show that they can be classified as a Type IIb SN (Krause et al. 2008; Rest et al. 2011), which originate from the core collapse of massive stars that have lost most of their hydrogen envelopes and consist of a nearly bare helium core at the time of its collapse. Thus the He core mass of the progenitor is supposed to be comparable to the stellar mass at the time of explosion, which is estimated as $\sim 5 \text{ M}_{\odot}$ by summing the masses of the ejecta and the neutron star. And the He core mass of $\sim 5 \text{ M}_{\odot}$ implies an initial mass of $\sim 16 \text{ M}_{\odot}$ (e.g., Woosley et al. 2002) with possibly a few tens percent of uncertainties. We note that this mass is close to the upper limit of Type II-P SNe ($\sim 15 \text{ M}_{\odot}$, Smartt et al. 2009). For a comparison, the progenitor star of the SN 1993J, the prototypical SN Type IIb, was a red supergiant (Nomoto et al. 1993, and references therein) with a main sequence mass probably in between 13 and 20 M_{\odot} (Woosley et al. 1994, and references therein).

Our analysis of the X-ray data suggests that Cas A has been expanding in a dense RSG wind whose swept-up mass is around 6 M_{\odot} . This large mass of swept-up RSG wind seems to indicate that the mass loss of the Cas A's progenitor might have been primarily via the RSG wind. However, stellar evolution models, with commonly adopted mass-loss rates for RSG stars (e.g., de Jager et al. 1988), predict significantly less mass loss via the RSG wind for a single $\sim 16 \text{ M}_{\odot}$ star (e.g., Woosley et al. 2002). For the progenitor of SN 1993J, the mass loss is attributed to Roche lobe overflow in the binary system (Stancliffe et al. 2009, and references therein). This was supported by the possible existence of a binary companion (Maund et al. 2004; Maund & Smartt 2009). A similar binary system also has been suggested for Cas A (e.g., Young et al. 2006), although no companion star has been currently identified. We note, however, that the mass loss rate of cool stars such as RSG stars is largely uncertain, and models may have underestimated the mass loss during the RSG phase. For example, stellar pulsations may trigger an unusually strong wind which substantially increases the mass loss rate in the RSG phase. Yoon et al. (2010) suggested that, if that happens, a single 20 M_{\odot} star can explode as a Type IIb SN after losing most of its hydrogen envelope.

6. COSMIC RAY ACCELERATION

So far we have neglected effects of cosmic ray acceleration in our analysis. However, the existence of X-ray nonthermal filaments around Cas A clearly indicates that electrons are accelerated up to the TeV energies. Observations also suggest that magnetic fields are amplified at the shock, which suggests the acceleration of cosmic ray protons (see Reynolds 2008, for a review). And modeling of the broadband nonthermal emission from the radio to the gamma-ray bands indicates acceleration of protons as well (e.g., Berezhko et al. 2003). Inclusion of cosmic ray acceleration will change the self-similar solutions we used, where a principal effect of efficient cosmic ray acceleration would be a reduction of the distances between the

forward shock and the reverse shock, as demonstrated in the Tycho SNR by Warren et al. (2005). However, the tendency of increasing density and decreasing temperature toward the contact discontinuity is not likely affected (Decourchelle et al. 2000). Thus, our conclusion that Cas A is expanding inside a wind would be valid even if cosmic acceleration were efficient in Cas A. On the other hand, we might have overestimated the wind density as the cosmic ray acceleration can increase the postshock gas compression ratio. For a strong relativistic shock, the compression ratio would be 7. The compression ratio will be further increased if accelerated cosmic rays efficiently escape the system.

We have assumed that the thermal emission we analyzed is from the postshock gas. In particular, we assumed that those regions we used for azimuthal analysis represents postshock gas right behind the forward shock. However, most of these regions are located beyond the nonthermal filaments that are the locations of forward shocks. We note that the intensity of the nonthermal filaments varies along the boundary, and it is particularly faint in the western boundary where the thermal emission is clearly seen. In this regard, we consider that the thermal emission beyond the nonthermal filaments are likely a projection of different shock fronts. It indicates that not all outer shocks of Cas A accelerate cosmic ray electrons efficiently enough to show X-ray nonthermal filaments. This further suggests that the mean expansion velocity of the shock front with nonthermal X-ray emission is slower than those without nonthermal X-ray emission. The slowing down of the shock might have been a consequence of efficient cosmic ray acceleration. In other words, there are regions where the acceleration has been less efficient, resulting in a larger shock radius that is sufficiently large to extend beyond the non-thermal filaments even in projection. This may be the case if the efficiency of CR acceleration depends on the angle between the shock normal and the magnetic field, as suggested for SN 1006 (Reynoso et al. 2013). On the other hand, it might be that the preshock condition necessary for efficient cosmic ray acceleration is related to the slowing down of the shock (e.g., density). Nevertheless, understanding differences of these shocks may provide valuable insight on the cosmic ray acceleration in the shocks.

7. SUMMARY

Using 1 Msec Chandra observation, we present our detailed analysis of the blast wave in the Galactic SNR Cas A. By analyzing the X-ray emission from the shocked

ambient gas, we have studied the nature of the ambient medium around Cas A, and also the nature of the progenitor star. Our results provide observational evidence of Cas A interacting with the RSG winds from the progenitor star.

- After removing spatially-varying background components, we identified faint emission, with no prominent limb-brightening, around the outer boundary of Cas A.
- X-ray spectra of these regions are well fit with the emission from a thermal plasma of subsolar abundances, indicating they are shocked ambient gas.
- In the western boundary where nonthermal emission is relatively weak, we extracted a radial series of spectra. Comparison with self-similar solutions of Chevalier (1982) indicates that Cas A is currently expanding inside a wind, rather than a uniform medium.
- The postshock density estimates from the spectra of the outermost shocked wind range between 3 and 5 cm⁻³, implying a preshock wind density of ~ 1 cm⁻³ at the current outer radius of Cas A (~ 3 pc). The high density of the wind suggests that it is a dense wind from a red supergiant (RSG) star.
- Combined with results of Chevalier & Oishi (2003), our measurements suggest that the ejected mass during the SN explosion was about $\sim 4 M_{\odot}$, implying total mass of the star (including the mass of the neutron star) at the explosion of $\sim 5 M_{\odot}$. Since Cas A was Type IIb SN (Krause et al. 2008), we estimate $\sim 16 M_{\odot}$ as the initial mass of the progenitor star.
- Estimated explosion energy of 5×10^{51} erg is larger than that of normal core-collapse SNe ($\sim 10^{51}$ erg), although not unprecedented for Type IIb SNe (Hamuy et al. 2009). On the other hand, the explosion energy would have been overestimated if wind density is overestimated.
- Our results suggest that the swept-up mass of the RSG wind is about $6 M_{\odot}$. This indicates that the progenitor of Cas A may have lost its mass primarily via the RSG wind.

REFERENCES

- Berezhko, E. G., Pühlhofer, G., & Völk, H. J. 2003, *A&A*, 400, 971
- Borkowski, K. J., Lyerly, W. J., & Reynolds, S. P. 2001, *ApJ*, 548, 820
- Chevalier, R. A. 1982, *ApJ*, 258, 790
- . 1999, *ApJ*, 511, 798
- . 2005, *ApJ*, 619, 839
- Chevalier, R. A., & Emmering, R. T. 1989, *ApJ*, 342, L75
- Chevalier, R. A., & Oishi, J. 2003, *ApJ*, 593, L23
- Churazov, E., Gilfanov, M., Forman, W., & Jones, C. 1996, *ApJ*, 471, 673
- de Jager, C., Nieuwenhuijzen, H., & van der Hucht, K. A. 1988, *A&AS*, 72, 259
- Decourchelle, A., Ellison, D. C., & Ballet, J. 2000, *ApJ*, 543, L57
- DeLaney, T., Rudnick, L., Fesen, R. A., Jones, T. W., Petre, R., & Morse, J. A. 2004, *ApJ*, 613, 343
- Favata, F., Vink, J., dal Fiume, D., Parmar, A. N., Santangelo, A., Mineo, T., Preite-Martinez, A., Kaastra, J. S., & Bleeker, J. A. M. 1997, *A&A*, 324, L49
- Ghavamian, P., Laming, J. M., & Rakowski, C. E. 2007, *ApJ*, 654, L69
- Hamuy, M., Deng, J., Mazzali, P. A., Morrell, N. I., Phillips, M. M., Roth, M., Gonzalez, S., Thomas-Osip, J., Krzeminski, W., Contreras, C., Maza, J., González, L., Huerta, L., Folatelli, G., Chornock, R., Filippenko, A. V., Persson, S. E., Freedman, W. L., Koviak, K., Suntzeff, N. B., & Krisciunas, K. 2009, *ApJ*, 703, 1612

- Hughes, J. P., Rakowski, C. E., Burrows, D. N., & Slane, P. O. 2000, *ApJ*, 528, L109
- Hwang, U., & Laming, J. M. 2009, *ApJ*, 703, 883
- . 2012, *ApJ*, 746, 130
- Hwang, U., Laming, J. M., Badenes, C., Berendse, F., Blondin, J., Cioffi, D., DeLaney, T., Dewey, D., Fesen, R., Flanagan, K. A., Fryer, C. L., Ghavamian, P., Hughes, J. P., Morse, J. A., Plucinsky, P. P., Petre, R., Pohl, M., Rudnick, L., Sankrit, R., Slane, P. O., Smith, R. K., Vink, J., & Warren, J. S. 2004, *ApJ*, 615, L117
- Krause, O., Birkmann, S. M., Usuda, T., Hattori, T., Goto, M., Rieke, G. H., & Misselt, K. A. 2008, *Science*, 320, 1195
- Laming, J. M., & Hwang, U. 2003, *ApJ*, 597, 347
- Lee, J., Park, S., Hughes, J. P., Slane, P. O., Gaensler, B. M., Ghavamian, P., & Burrows, D. N. 2010, *ApJ*, 711, 861
- Maeder, A., Meynet, & G. 2000, *A&A*, 361, 159
- Mauche, C. W., & Gorenstein, P. 1989, *ApJ*, 336, 843
- Maund, J. R., & Smartt, S. J. 2009, *Science*, 324, 486
- Maund, J. R., Smartt, S. J., Kudritzki, R. P., Podsiadlowski, P., & Gilmore, G. F. 2004, *Nature*, 427, 129
- Nomoto, K., Suzuki, T., Shigeyama, T., Kumagai, S., Yamaoka, H., & Saio, H. 1993, *Nature*, 364, 507
- Overbeck, J. W. 1965, *ApJ*, 141, 864
- Predehl, P., & Schmitt, J. H. M. M. 1995, *A&A*, 293, 889
- Reed, J. E., Hester, J. J., Fabian, A. C., & Winkler, P. F. 1995, *ApJ*, 440, 706
- Rest, A., Foley, R. J., Sinnott, B., Welch, D. L., Badenes, C., Filippenko, A. V., Bergmann, M., Bhatti, W. A., Blondin, S., Challis, P., Damke, G., Finley, H., Huber, M. E., Kasen, D., Kirshner, R. P., Matheson, T., Mazzali, P., Minniti, D., Nakajima, R., Narayan, G., Olsen, K., Sauer, D., Smith, R. C., & Suntzeff, N. B. 2011, *ApJ*, 732, 3
- Reynolds, S. P. 2008, *ARA&A*, 46, 89
- Reynoso, E. M., Hughes, J. P., & Moffett, D. A. 2013, *AJ*, 145, 104
- Schure, K. M., Vink, J., García-Segura, G., & Achterberg, A. 2008, *ApJ*, 686, 399
- Smartt, S. J., Eldridge, J. J., Crockett, R. M., & Maund, J. R. 2009, *Mon. Not. R. Astron. Soc.*, 395, 1409
- Smith, N., Li, W., Filippenko, A. V., & Chornock, R. 2011, *Mon. Not. R. Astron. Soc.*, 412, 1522
- Sramek, R. A., & Weiler, K. W. 2003, in *Lecture Notes in Physics*, Berlin Springer Verlag, Vol. 598, Supernovae and Gamma-Ray Bursters, ed. K. Weiler, 145–169
- Stancliffe, J. R., Eldridge, & J. J. 2009, *Mon. Not. R. Astron. Soc.*, 396, 1699
- Sugerman, B. E. K., Crotts, A. P. S., Kunkel, W. E., Heathcote, S. R., & Lawrence, S. S. 2005, *ApJ*, 627, 888
- Thorstensen, J. R., Fesen, R. A., & van den Bergh, S. 2001, *AJ*, 122, 297
- Vink, J., Kaastra, J. S., & Bleeker, J. A. M. 1996, *A&A*, 307, L41
- Vink, J., & Laming, J. M. 2003, *ApJ*, 584, 758
- Warren, J. S., Hughes, J. P., Badenes, C., Ghavamian, P., McKee, C. F., Moffett, D., Plucinsky, P. P., Rakowski, C., Reynoso, E., & Slane, P. 2005, *ApJ*, 634, 376
- Woosley, S. E., Eastman, R. G., Weaver, T. A., & Pinto, P. A. 1994, *ApJ*, 429, 300
- Woosley, S. E., Heger, A., & Weaver, T. A. 2002, *Rev. Mod. Phys.*, 74, 1015
- Yoon, S.-C., Cantiello, & M. 2010, *ApJ*, 717, L62
- Young, P. A., Fryer, C. L., Hungerford, A., Arnett, D., Rockefeller, G., Timmes, F. X., Voit, B., Meakin, C., & Eriksen, K. A. 2006, *ApJ*, 640, 891